Scripta Materialia 263 (2025) 116664

Contents lists available at ScienceDirect

Scripta Materialia

journal homepage: www.journals.elsevier.com/scripta-materialia

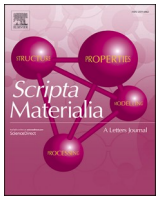

X-ray tomography analysis of intermetallics and voids in 6XXX alloys

Tristan Kammbach [a], Elisa Cantergiani [b], Tillmann R. Neu [a], Paul H. Kamm [a], Jonathan Friedli [b], Zeqin Liang [b], Francisco García-Moreno [a,*]

[a] Helmholtz-Zentrum Berlin für Materialien und Energie, Hahn-Meitner-Platz 1, Berlin 14109, Germany
[b] Novelis Switzerland SA, Rte des Laminoirs 15, Sierre 3960, Switzerland

ARTICLE INFO

Keywords:
X-ray Tomography
Aluminum
Recycled alloy
Intermetallics
Voids

ABSTRACT

Sustainable aluminum production for the automotive industry with a high content of recycled material offers considerable potential for CO_2 footprint reduction and cost savings. A three-dimensional characterization of cast AA6016 alloys with <50 wt% and >75 wt% of recycled aluminum was carried out to assess the volume fraction, total number and surface area of intermetallics and casting voids using high-resolution synchrotron X-ray tomography. A new data analysis method is presented to describe morphology of intermetallics based on a surface area/volume by volume plot, which allows for better classification of their different geometry clusters even for small modifications of Fe and Mn in the cast alloy.

The economic importance and environmental benefits of maximizing the recycling of aluminum have been discussed for several decades [1]. A closed recycling loop for aluminum from vehicles at the end of their useful life is an important goal for sustainable production [2,3]. New technologies are emerging for the development and industrial use of sensor-based scrap sorting processes for the separation of wrought alloys by alloy type in large quantities [4]. Producers are encouraged to use more aluminum scrap sources, to lead to a significant CO_2 reduction [5], but impurities, especially Fe, in the recycled aluminum alloy can cause an increased number of detrimental intermetallic components [6–14]. The latter can lower the strength and ductility in the casting and worsen sheet bending performances, especially for high percentages of scrap content [15–17]. On the other hand, it is possible to engineer the intermetallic phases in such a way that they have a positive influence on the mechanical properties during certain temperature treatments [18–20]. To satisfy the requirements of the automotive industry, the formation of detrimental intermetallic compounds in cast primary and recycled material as well as their influence on the mechanical performance of the alloys must be understood and controlled. For the common analysis of voids and intermetallic compounds, SEM or TEM methods are used, which provide a 2D image of the morphology with sufficient spatial resolution but insufficient statistical relevance [21–23]

Over the last few decades, 3D X-ray computed tomography (X-CT) has developed into a very powerful tool for analyzing the internal structure of matter [24–26]. This method has been successfully used in the past to investigate various aluminum alloys and to gain further insights into the spatial relationships between the voids and the intermetallic constituents [24,26–29]. In this work we apply synchrotron X-ray tomography to study in detail and quantitatively compare the 3D morphology of particles and voids in AA6016 samples produced from primary and recycled aluminum. The aim is to obtain comprehensive statistical 3D data, which can hardly be obtained from individual 2D electron microscopy measurements, in order to characterize the volume fraction of intermetallics and voids, the surface, shape, distribution and network arrangement, demonstrating the potential and advantages of the method. This knowledge can help tailor the production process to minimize the impact of high amounts of recycled aluminum on alloy performance.

Cylindrical samples of dimensions $1-3$ mm in diameter and $2-10$ mm in length of the commercial alloy AA6016 used by the automotive industry and provided by Novelis Switzerland SA were prepared from direct chill (DC) casted ingots. High-resolution synchrotron X-CT was performed at the TOMCAT beamline of the Paul Scherer Institute, Villigen, Switzerland. The experimental setup, where a cylindrical sample is placed on a rotation stage and the X-ray intensities transmitted through the sample are converted into light by a 20 μm-thick LuAG:Ce scintillator, is shown in Fig. S1. The projections are transferred by a 10x optical microscope to a sCMOS camera (pco.edge 5.5, PCO, Kehlheim, Germany) and recorded. With a monochromatic beam of 21 keV, 2000 projections per tomogram, an effective pixel size of 0.65 μm, a field of

* Corresponding author.
E-mail address: garcia-moreno@helmholtz-berlin.de (F. García-Moreno).

https://doi.org/10.1016/j.scriptamat.2025.116664
Received 20 December 2024; Received in revised form 17 March 2025; Accepted 20 March 2025
Available online 28 March 2025

view of 2560 × 2160 pixels and an exposure time of 250 ms per projection, tomograms were acquired in around 9 min per sample by rotating them over 180°. The spatial resolution was in the range of 1.3 − 1.5 μm, sufficient to observe a large number of casting voids and intermetallics in the analysed volume of 1.5 mm × 1.5 mm × 1.4 mm.

The recorded projections were corrected with previously recorded flat and dark fields and a single-distance phase retrieval method was applied to reduce the edge enhancement and increase the contrast of the images based on the complex refractive index [30]. For this purpose, the parameters $\delta = 10^{-7}$ and $\beta = 10^{-9}$ were used at a distance of 10 mm. The tomographic reconstruction was performed using the Gridrec algorithm [31].

To demonstrate the potential of the method we studied quantitatively the size distributions, volume fractions, total number of intermetallics and casting voids, surface area and network structure of the commercial AA6016 alloy with low recycling content (<50 wt%) and a modifiedAA6016-RC alloy with high recycling content (>75 wt%) containing 0.3 wt% Fe and up to 0.2 wt% Mn depending on the scrap availability in the DC casting condition The composition of the alloys can be found in Table 1. This characterization will allow for a better comparison and a finer adjustment of production parameters to modify the morphology of the intermetallics or avoid negative effects on material quality.

To prepare the reconstructed volumes for segmentation two distinct approaches were taken:

(1) The segmentation for fine detail was initiated by a difference of Gaussians (DoG) filtering which was performed in ImageJ [32]. There, a 3D Gaussian blur ($\sigma = 43$, $\mu = 1$) of the original volume was created and reduced by 0.05 times of its mean value. The resulting offset Gaussian blur was then subtracted from the original volume to create the DoG volume. To suppress the side effect of bloom at the interfaces between low absorbing regions (voids) and matrix, the former were segmented from the gaussian blur image by thresholding. The segmented void volumes were subsequently dilated 7 times with a 3 × 3 × 3 kernel and subtracted from the DoG volume. Following this preparatory step, images were further analyzed with the software Dragonfly 3D World (Comet Technologies Canada Inc, version: 2024.1.0.1597) [33]. Particles were segmented from the DoG volume by manually thresholding the volume, gradually approaching increasing threshold intensities until the background noise was excluded. The voids were segmented from the unfiltered, reconstructed volume as the contrast between voids and matrix was much higher.
(2) In the segmentation for quantitative analysis the DoG filter was substituted for the slope map filter from Dragonfly 3D World. Using this approach, finer details were suppressed due to some residual bloom around the particles, which allowed for an overall more stable quantitative analysis of volume fractions and total surface.

To further prevent noise from interfering with the segmentation, in both segmentations, connected regions below a volume of 5 voxels were discarded. Voids and particles were masked by a cylindrical region of interest to remove local tomography artifacts in the outer region caused by contributions from the external volume. Volume fractions were obtained by comparing the voxels labeled as particles and voids with the cylindrical region of interest. The individual objects were labeled using a 26-connected kernel and their individual volumes and surface areas [34] calculated to depict their distributions. All rendered volumes were displayed in orthographic projection.

Table 1
Chemical composition (wt. %) of major alloying elements in the samples used in this study.

Alloy	Si	Mg	Fe	Mn	Cr
AA6016	1.2	0.4	0.2	0.08	0.04
AA6016RC	1.2	0.4	0.3	0.15	0.04

Complementary scanning electron microscopy (SEM) and energy dispersive X-ray spectroscopy (EDX) were performed on the samples to show in detail different compositions and morphologies of the particles and compare them with the tomographic results. The area fraction of the Fe-containing intermetallics was acquired by simple thresholding of the corresponding particles.

SEM and EDX performed on AA6016 and AA6016-RC samples show different AlFeSi intermetallics phases and their morphology and voids (see Fig. 1). The comparison between both alloys shows slight differences between the amount of intermetallics. By analyzing several 2D SEM images similar to the ones shown in Fig. 1(a) and (b), the percentage of 2D surface area of Fe-containing intermetallics without distinction between the phase type (i.e. if α- or β-AlFeSi) could be estimated to 0.97±0.12% for AA6016 and 1.2 ± 0.2% for AA6016-RC by thresholding, indicating a higher amount of Fe-containing intermetallics in the recycled alloy. Nonetheless, this standard method has some limitations as i) it needs a large number of single images taken in different zones of the sample, ii) it provides area fractions instead of volume fractions as e.g. given by simulations, iii) it assumes a relative homogeneous distribution of the particles, iv) it does not give information about the real 3D shapes and sizes of the particles but only a cross section and v) it does not take into account superordinated network structures such as cluster of particles.

To obtain a more precise evaluation of the morphology, 3D X-CT was performed, whose contrast and spatial resolution is sufficient to resolve voids and Fe-containing intermetallics. Fig. 2(a) and (b) show representative slices extracted from a tomographic volume comparing the 2D structure of voids and intermetallics for AA6016 and AA6016-RC, respectively. Similar to SEM images slight differences of more pronounced intermetallics for AA6016-RC can be observed, a condition that is found all over the scanned volume. Fig. 2(c) and (d) show a magnified view of single intermetallic particles selected for both conditions. The spatial resolution allows for a detailed observation of their morphology, which allows them to be identified as α-phase intermetallics. Casting voids are predominantly found attached to intermetallics in both cases, but not always (see Fig. 1(c) and (d) and Fig. 2(c) and (d)).

A segmentation step to separate the intermetallics and voids from the aluminum matrix was applied to the tomographic volume datasets. Fig. 2(e) and (f) show the interconnection of segmented intermetallic particles projected to a single slice as red overlay. There, we can observe that most of the supposedly unconnected intermetallics in 2D are interconnected in 3D, which emphasizes the need for 3D evaluations. The corresponding intermetallic networks of β-AlFeSi and α-AlFeSi particles are shown in 3D in Fig. 2(g) and (h), respectively. In general, α-particles are rounder than β-particles which appear as thin plates (needle shape in 2D analyses). For a more detailed identification of the individual phases with their atomic composition or their crystal structure, an approach as shown by Kral would be required [35].

An accurate comparison of the morphology of the individual intermetallic particles reveals major differences. Most particles contained in the alloy with low amount of recycled material have a spindly structure consisting of thin, elongated and slightly curved plates. These plates form a complex network in which several of them are often connected in nodes. In many sections there are thin square plates attached to the long plates (Fig. 2(g)). The thinnest dimension of any submorphology rarely surpasses 2 μm, with even thicker sections of intermetallics remaining below 5 μm. They are β-phase AlFeSi when compared to the SEM images (Fig. 1), where their overall shape corresponds to square or elongated platelets [36]. Coexisting with this prevalent morphology is a second morphology. The intermetallics belonging to this specific habit form in flat lamellae with a ribbed inner structure, which often form star-shaped in 3 or 4 lamellae around a central nucleation site, which can be best

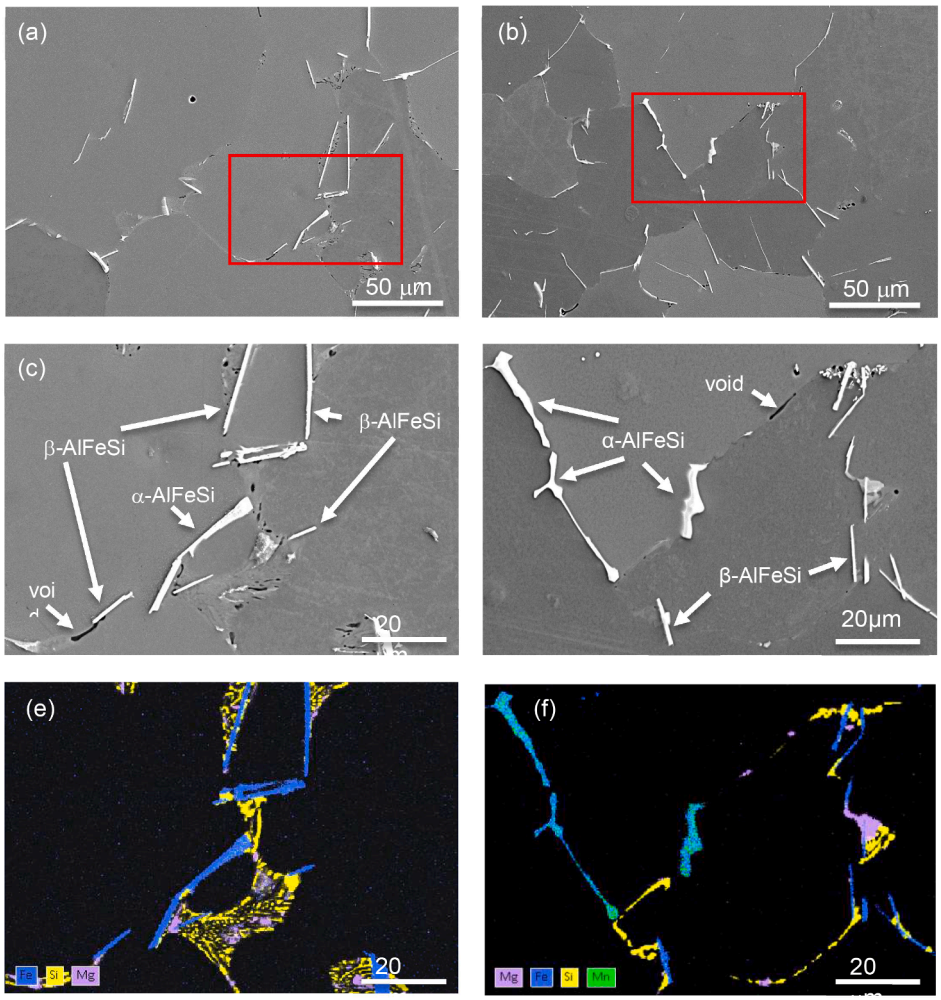

Fig. 1. SEM images of AA6016, (a) with low and (b) with high amount of recycled material. (c) and (d) are magnified images showing a more detailed view of voids and intermetallic particles in the region marked with a red square in (a) and (b). Different α-AlFeSi and β-AlFeSi intermetallic particles and voids are indicated. (e) and (f) are the corresponding EDX maps of Fe (blue), Mn (green), Mg (pink) and Si (yellow). Manganese contents in (e) did not surpass the detection limit and thus were omitted.

observed in AA6016-RC (Fig. 2(h)). The comparison with SEM images confirms this particle morphology as α-AlFeSi particle matching with morphologies investigated by Lui et al. using SEM imaging on etched-free intermetallics [37].

While α-AlFeSi and β-AlFeSi intermetallics are present in the AA6016 alloy, AA6016-RC is dominated by a more interconnected network of the larger and bulkier α-phase intermetallics. In general, both morphologies can be found in either sample, however their respective quantities and network arrangement differ. Moreover, the alloy AA6016-RC has a higher content of manganese coming from scrap sources, which stabilizes the α-AlFeSi during casting solidification when it would mostly form as β-AlFeSi without it [38,39]. Many studies have reported the effect of manganese in the stabilization of α-AlFeSi [40–45].

Fig. 3 reveals that the majority of all intermetallic particles and also voids are arranged in networks, which can be only identified in 3D. The volume of a single sample measured with tomography is 3 mm^3, which cannot realistically be achieved with an SEM slide-by-slide examination, and it is larger than previously analyzed 3D volumes [18–20].

The voids in AA6016-RC are double in volume (0.1 vol% vs 0.05 vol %) but distributed in smaller individual larger volumes as compared to AA6016, where large voids form fewer but larger local clusters between grain boundaries attached to intermetallics as can be observed in Fig. 3 (e) and (f). However, it is assumed that the void volume and network configuration in the alloys might have no influence, as the pores will be closed during the subsequent hot rolling process.

In Fig. 4(a) and (b), we can observe the area fraction of intermetallic particles distributed over the whole sample height and obtained from the tomographic slices of (a) AA6016 and (b) AA6016-RC. This analysis simulates the results which are usually obtained from single SEM images. The large standard deviation (>50% of the mean value) shows the inaccuracy of such an approach depending on the position in the sample, because intermetallics particles are often connected in clusters and locally not homogeneously distributed. This serves to explain the difference in area fraction between X-CT and SEM because the area fraction is highly dependent on the position it was taken from. This is reinforced by the evidence that the volume fraction was calculated based on a segmentation where the fine structures were obscured and thus comparatively over-segmented. To mitigate this effect, the choice of the segmentation approach becomes an important factor to consider. Particularly, machine learning based methods could provide for a higher degree of detail at the cost of up-front time investment. Fig. 4(c) and (d) show the histogram of the absolute volumes of individual clusters (in green) next to their volume over surface as a shape factor (in light blue) for AA6016 and AA6016-RC based on DoG segmentation. Observing the scatter plot of the clusters in this parameter window (dark blue dots), we can observe 3 different types of intermetallic cluster populations, with different volume/surface in AA6016: type 1, 2 and 3 with large, low and medium volume/surface ratio, respectively, as shown in Fig. 4c). In

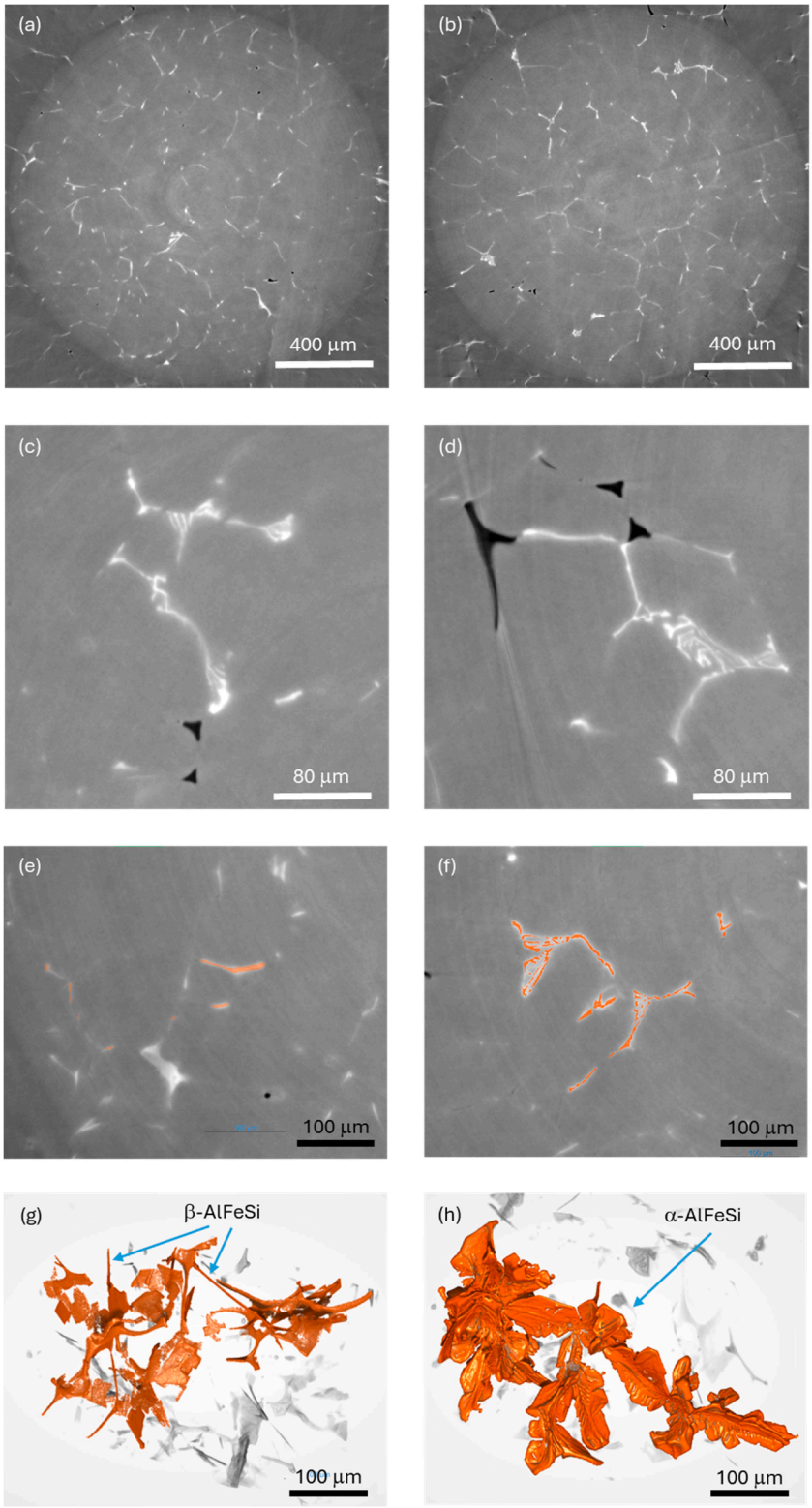

Fig. 2. Reconstructed tomographic slices extracted from 3D tomograms of AA6016 alloy made (a) with low and (b) with high content of recycled material. Intermetallics can be observed in white, voids in black. (c) and (d) are magnified views showing a more detailed view of voids and of the intermetallic particles. The typical morphology of α-phase intermetallic particles (α-AlFeSi) can be observed. (e) and (f) show segmented intermetallics (in red) in both alloys which seem not to be interconnected, but (g) and (h) show in 3D that they are actually interconnected by a network of several hundreds of micrometer length.

AA6016-RC the type 2 cluster is more pronounced than in AA6016 and type 3 is almost not present (see Fig. 4d)), which can be attributed to the low presence of the β-AlFeSi phases in alloys with high recycled amount of material.

A quantitative analysis of the segmented intermetallics and voids with calculation of their volume percentage and total surface is presented in Table 2. We can observe that the volume fraction of all intermetallics measured by 3D X-CT is ~40% larger in the sample

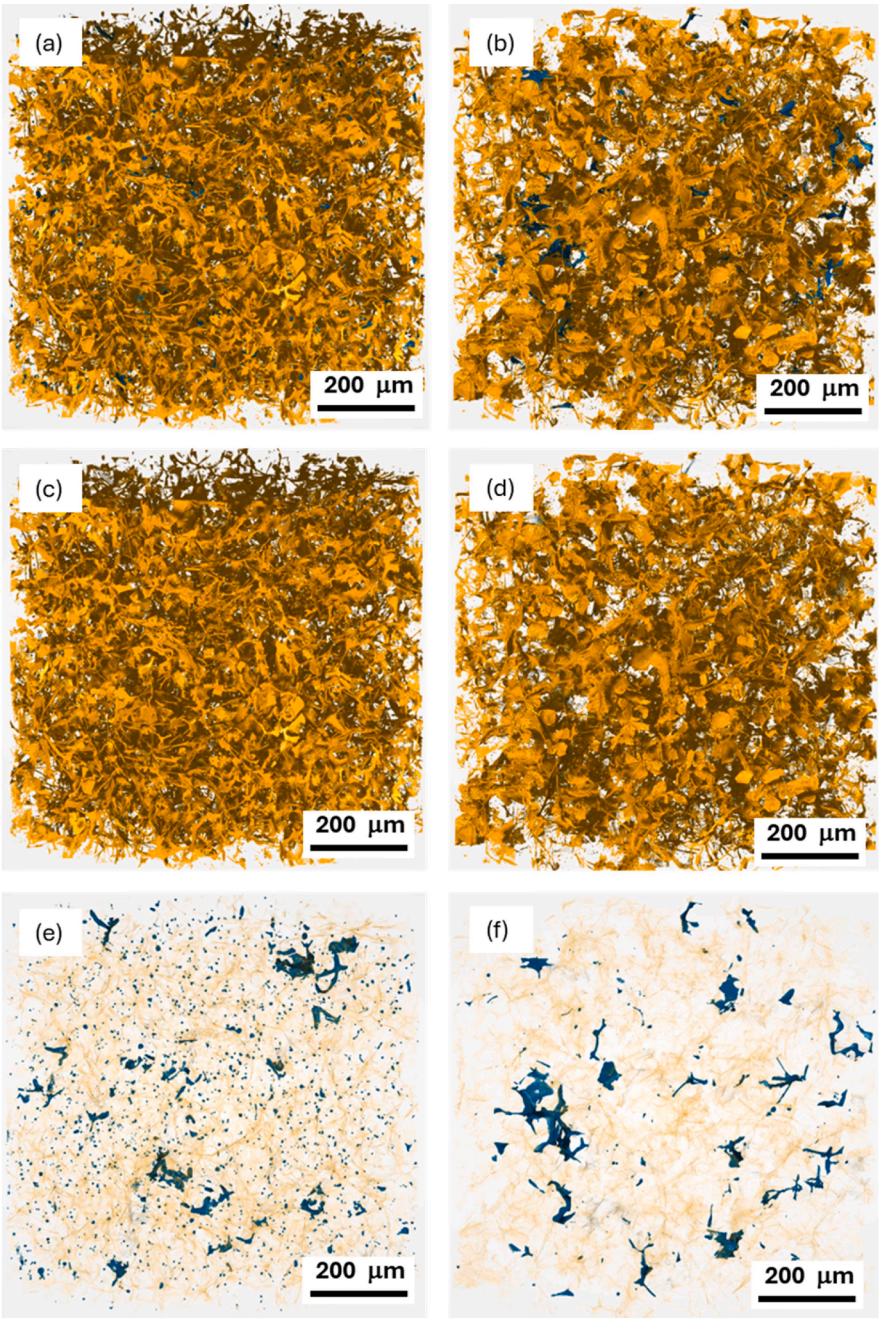

Fig. 3. 3D reconstructed rendering of tomograms of AA6016 alloy made (a), (c) and (e) with low and (b), (d) and (f) with high amount of recycled material showing voids in blue and the intermetallics in yellow. Interconnected particles and voids show different network structures.

containing a higher amount of recycled material (i.e. higher Fe content). On the other hand, the intermetallics interface is ~27% lower in AA6016-RC, which can be attributed to the broader morphology of the particles and a stronger bonding between them in this alloy. This may also contribute to the fact that AA6016-RC can exhibit similarly good mechanical properties to AA6016 despite a higher intermetallic volume fraction. While the 2D analysis of the 2D X-CT slices provides very similar values due to extensive statistical data, the conventional 2D SEM analysis of the same sample obtained from 3 images of different regions underestimates in this case the volume fraction of intermetallics and varies considerably depending on the region of the sample the images are taken from (see Fig. 4(a) and (b)). The large standard deviation in the 2D analysis of the 2D X-CT slices emphasizes the need for 3D analysis.

The influence of the type of cluster structure besides the volume percentage and type of intermetallics on alloy performance needs to be studied as well as how to modify them during casting and successive homogenization and hot rolling. Controlling morphology and precipitating phase during the whole aluminum sheet processing is fundamental as microvoids and intermetallics have a direct effect on bending performance for hemming in automotive products.

We can conclude that:

- 3D synchrotron X-ray tomography is a powerful characterization tool to image in 3D voids and intermetallics in Al-alloys, enabling the observation of particle clusters and their network configuration as well as better statistics of the volume fraction compared to conventional SEM 2D analyses.

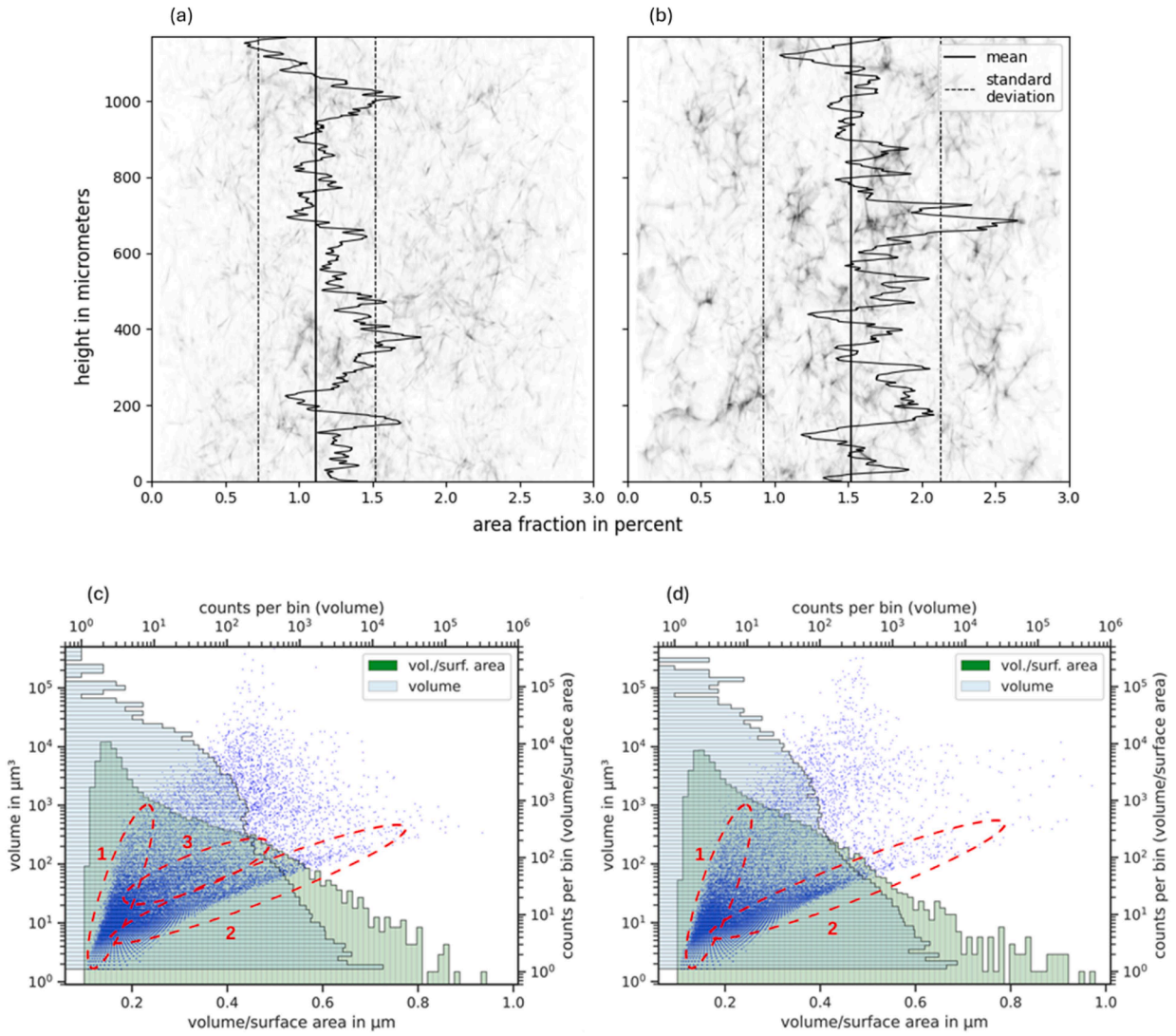

Fig. 4. Area fraction of intermetallic particles over the sample height of (a) AA6016 and (b) AA6016-RC obtained from 2D tomographic slices. Volume (in cyan) and surface area (in green) distribution of intermetallic clusters as well as their distribution relative to their own surface (blue dots) for (c) AA6016 and (d) AA6016-RC obtained from 3D tomographic volumes.

Table 2
Quantitative analysis of volume and surface of intermetallics and volume of voids for AA6016 and AA6016-RC and corresponding standard deviations extracted from the 2D SEM images (see Fig. 1), from the 2D X-CT slices (see Fig. 4) and from the 3D X-CT tomographic volumes (see Fig. 3).

Parameter (Method)	AA6016	AA6016 St. dev.	AA6016-RC	AA6016-RC St. dev.
Interm. area fract. (2D SEM) [%]	0.97	0.12	1.2	0.21
Interm. area fract. (2D X-CT) [%]	1.12	0.40	1.52	0.60
Interm. vol. fract. (3D X-CT) [%]	1.14	–	1.6	–
Interm. surf. /vol. fract. (3D X-CT) [mm^2/mm^3]	674	–	491	–
Voids vol. fract. (3D X-CT) [vol%]	0.05	–	0.1	–

- AA6016-RC has a larger volume fraction of voids and intermetallics as well as a size distributions of clusters of interconnected intermetallics shifted to larger volumes compared to AA6016.
- The proposed volume/surface area analysis is an efficient method to highlight difference in the distribution of intermetallics clusters. Three different cluster types of intermetallics were identified in AA6016. In AA6016-RC the type 2 cluster is much more pronounced than in AA6016, and type 3 is almost absent, indicating less β-AlFeSi phases. This suggests that although there is more Fe in AA6016-RC than in AA6016, the number of β-AlFeSi phases is lower due to a higher Mn content.

CRediT authorship contribution statement

Tristan Kammbach: Writing – review & editing, Writing – original draft, Visualization, Validation, Software, Methodology, Investigation, Formal analysis, Data curation, Conceptualization. **Elisa Cantergiani:** Writing – review & editing, Validation, Investigation, Data curation, Conceptualization. **Tillmann R. Neu:** Methodology, Investigation, Data curation, Conceptualization. **Paul H. Kamm:** Writing – review & editing, Software, Methodology, Investigation, Data curation. **Jonathan Friedli:** Project administration, Conceptualization. **Zeqin Liang:** Writing – review & editing, Validation, Supervision, Resources, Project

administration, Investigation, Conceptualization. **Francisco García-Moreno:** Writing – review & editing, Writing – original draft, Validation, Supervision, Resources, Project administration, Funding acquisition, Conceptualization.

Declaration of competing interest

The authors declare that they have no known competing financial interests or personal relationships that could have appeared to influence the work reported in this paper.

Acknowledgments

We acknowledge the Paul Scherrer Institute, Villigen, Switzerland for the provision of synchrotron radiation beamtime at the TOMCAT beamline X02DA of the SLS. Furthermore, we acknowledge Erika Zaiser for her helpful assistance in acquiring the SEM image and Christian Menzel for the sample preparation.

Supplementary materials

Supplementary material associated with this article can be found, in the online version, at doi:10.1016/j.scriptamat.2025.116664.

References

[1] S.K. Das, Designing aluminium alloys for a recycling friendly world, Mater. Sci. Forum 519-521 (2006) 1239–1244.
[2] J.L. Cann, A. De Luca, D.C. Dunand, D. Dye, D.B. Miracle, H.S. Oh, E.A. Olivetti, T. M. Pollock, W.J. Poole, R. Yang, C.C. Tasan, Sustainability through alloy design: challenges and opportunities, Prog. Mater. Sci. 117 (2021) 100722.
[3] D. Raabe, D. Ponge, P.J. Uggowitzer, M. Roscher, M. Paolantonio, C. Liu, H. Antrekowitsch, E. Kozeschnik, D. Seidmann, B. Gault, F. De Geuser, A. Deschamps, C. Hutchinson, C. Liu, Z. Li, P. Prangnell, J. Robson, P. Shanthraj, S. Vakili, C. Sinclair, L. Bourgeois, S. Pogatscher, Making sustainable aluminum by recycling scrap: the science of "dirty" alloys, Prog. Mater. Sci. 128 (2022) 100947.
[4] S. Van den Eynde, E. Bracquené, D. Diaz-Romero, I. Zaplana, B. Engelen, J. R. Duflou, J.R. Peeters, Forecasting global aluminium flows to demonstrate the need for improved sorting and recycling methods, Waste Manage. 137 (2022) 231–240.
[5] J. Pedneault, G. Majeau-Bettez, M. Margni, How much sorting is required for a circular low carbon aluminum economy? J. Ind. Ecol. 27 (3) (2023) 977–992.
[6] J. Kim, D. Kim, Effects of fragmented Fe intermetallic compounds on ductility in Al-Si-Mg alloys, J. Nanosci. Nanotechnol. 18 (3) (2018) 2137–2139.
[7] E. Cinkilic, C.D. Ridgeway, X. Yan, A.A. Luo, A Formation map of iron-containing intermetallic phases in recycled cast aluminum alloys, Metall. Mater. Trans. A 50 (12) (2019) 5945–5956.
[8] W. Khalifa, F.H. Samuel, U. Gm Nserc, J.E. Gruzleski, H.W. Doty, S. Valtierra, Nucleation of Fe-intermetallic phases in the Al-Si-Fe alloys, Metall. Mater. Trans A 36 (4) (2005) 1017–1032.
[9] Z. Que, Y. Wang, Z. Fan, Formation of the Fe-Containing Intermetallic Compounds during Solidification of Al-5Mg-2Si-0.7Mn-1.1Fe Alloy, Metall. Mater. Trans. A 49 (6) (2018) 2173–2181.
[10] M.A. Moustafa, Effect of iron content on the formation of β-Al5FeSi and porosity in Al–Si eutectic alloys, J. Mater. Process. Technol. 209 (1) (2009) 605–610.
[11] Z. Jin, C. Cai, T. Hashimoto, Y. Yuan, D. Kang, J. Hunter, X. Zhou, The behaviour of iron-containing intermetallic particles in aluminium alloys in alkaline solution, Corros. Sci. 179 (2021) 109134.
[12] J. Grasserbauer, I. Weißensteiner, G. Falkinger, T.M. Kremmer, P.J. Uggowitzer, S. Pogatscher, Influence of Fe and Mn on the microstructure formation in 5xxx alloys—Part I: evolution of primary and secondary phases, Materials (2021).
[13] J.A. Taylor, Iron-Containing intermetallic phases in Al-Si based casting alloys, Procedia Mater. Sci. 1 (2012) 19–33.
[14] L.F. Mondolfo, Aluminum Alloys: structure and Properties, Elsevier Sci. (2013).
[15] D. De Caro, M.M. Tedesco, J. Pujante, A. Bongiovanni, G. Sbrega, M. Baricco, P. Rizzi, Effect of recycling on the mechanical properties of 6000 series aluminum-alloy sheet, Materials (2023).
[16] A. Bjurenstedt, E. Ghassemali, S. Seifeddine, A.K. Dahle, The effect of Fe-rich intermetallics on crack initiation in cast aluminium: an in-situ tensile study, Mater. Sci. Eng., A 756 (2019) 502–507.
[17] S. Ji, W. Yang, F. Gao, D. Watson, Z. Fan, Effect of iron on the microstructure and mechanical property of Al–Mg–Si–Mn and Al–Mg–Si diecast alloys, Mater. Sci. Eng., A 564 (2013) 130–139.
[18] Y. Zhao, W. He, J. Medina, D. Song, Z. Sun, Y. Xue, G. González-Doncel, R. Fernández, Contribution of the Fe-rich phase particles to the high temperature mechanical behaviour of an Al-Cu-Fe alloy, J. Alloys. Compd. 973 (2024) 172866.
[19] Y. Zhao, W. He, F. Zhao, C. Song, W. Zhang, D. Song, Y. Tang, Z. Sun, W. Yin, Y. Xue, R. Li, R. Fernández, Insight into the Fe-rich phases strengthening mechanisms of non-heat-treatable Al-Mg-Mn-Fe-Cu alloys, J. Mater. Sci. Technol. 205 (2025) 232–246.
[20] Y. Zhao, D. Song, H. Wang, Y. Jia, B. Lin, Y. Tang, Y. Tang, D. Shu, Z. Sun, Y. Fu, W. Zhang, Revealing the influence of Fe on Fe-rich phases formation and mechanical properties of cast Al-Mg-Mn-Fe alloys, J. Alloys. Compd. 901 (2022) 163666.
[21] N.C.W. Kuijpers, W.H. Kool, P.T.G. Koenis, K.E. Nilsen, I. Todd, S. van der Zwaag, Assessment of different techniques for quantification of α-Al(FeMn)Si and β-AlFeSi intermetallics in AA 6xxx alloys, Mater. Charact. 49 (5) (2002) 409–420.
[22] G. Sha, K. O'Reilly, B. Cantor, Characterization of Fe-rich intermetallic phases in a 6xxx series Al alloy, Mater. Sci. Forum 519-521 (2006) 1721–1726.
[23] N.C.W. Kuijpers, J. Tirel, D.N. Hanlon, S. van der Zwaag, Quantification of the evolution of the 3D intermetallic structure in a 6005A aluminium alloy during a homogenisation treatment, Mater. Charact. 48 (5) (2002) 379–392.
[24] F. García-Moreno, T.R. Neu, P.H. Kamm, J. Banhart, X-ray tomography and tomoscopy on metals: a review, Adv. Eng. Mater. 25 (2023) 2201355.
[25] P.J. Withers, C. Bouman, S. Carmignato, V. Cnudde, D. Grimaldi, C.K. Hagen, E. Maire, M. Manley, A. Du Plessis, S.R. Stock, X-ray computed tomography, Nat. Rev. Methods Primers. 1 (1) (2021) 18.
[26] J. Alkemper, P.W. Voorhees, Three-dimensional characterization of dendritic microstructures, Acta Mater. 49 (5) (2001) 897–902.
[27] Y. Zhao, Z. Wang, C. Zhang, W. Zhang, Synchrotron X-ray tomography investigation of 3D morphologies of intermetallic phases and pores and their effect on the mechanical properties of cast Al-Cu alloys, J. Alloys. Compd. 777 (2019) 1054–1065.
[28] D. Kim, J. Kim, E. Kobayashi, Microstructure characterization of rolled Al-Si-Mg-Fe alloy by three-dimensional tomography, Mater. Sci. Eng., A 768 (2019) 138449.
[29] S. Terzi, J.A. Taylor, Y.H. Cho, L. Salvo, M. Suéry, E. Boller, A.K. Dahle, In situ study of nucleation and growth of the irregular α-Al/β-Al5FeSi eutectic by 3-D synchrotron X-ray microtomography, Acta Mater. 58 (16) (2010) 5370–5380.
[30] D. Paganin, S.C. Mayo, T.E. Gureyev, P.R. Miller, S.W. Wilkins, Simultaneous phase and amplitude extraction from a single defocused image of a homogeneous object, J. Microsc. 206 (1) (2002) 33–40.
[31] F. Marone, M. Stampanoni, Regridding reconstruction algorithm for real-time tomographic imaging, J. Synchrotron Rad. 19 (6) (2012) 1029–1037.
[32] J. Schindelin, I. Arganda-Carreras, E. Frise, V. Kaynig, M. Longair, T. Pietzsch, S. Preibisch, C. Rueden, S. Saalfeld, B. Schmid, J.-Y. Tinevez, D.J. White, V. Hartenstein, K. Eliceiri, P. Tomancak, A. Cardona, Fiji: an open-source platform for biological-image analysis, Nat. Methods 9 (7) (2012) 676–682.
[33] O.R. Systems, Dragonfly 3D World, 2024. https://dragonfly.comet.tech/en/product-overview/dragonfly-3d-world. (Accessed 8. July 2024).
[34] J. Lindblad, Surface area estimation of digitized 3D objects using weighted local configurations, Image Vis. Comput. 23 (2) (2005) 111–122.
[35] M.V. Kral, A crystallographic identification of intermetallic phases in Al–Si alloys, Mater. Lett. 59 (18) (2005) 2271–2276.
[36] C. Romming, V. Hansen, J. Gjonnes, Crystal structure of [beta]-Al4.5FeSi, Acta Crystallographica Sect. B 50 (3) (1994) 307–312.
[37] A. Lui, P.S. Grant, I.C. Stone, K.A.Q. O'Reilly, The Role of Grain Refiner in the Nucleation of AlFeSi Intermetallic Phases During Solidification of a 6xxx Aluminum Alloy, Metall. Mater. Trans. A 50 (11) (2019) 5242–5252.
[38] O. Engler, T. Schröter, C. Krause, Formation of intermetallic particles during solidification and homogenisation of two Al–Mg–Si alloys, Mater. Sci. Tech. 39 (1) (2023) 70–84.
[39] Tribunskii, A. & Aryshenskii, E. & Nosova, E. & Chinov, V., Evolution of the Size and Number of Intermetallic Particles in the Production of.
[40] S.G. Shabestari, The effect of iron and manganese on the formation of intermetallic compounds in aluminum–silicon alloys, Mater. Sci. Eng., A 383 (2) (2004) 289–298.
[41] R. Podprocká, D. Bolibruchová, The role of manganese in the alloy based on Al-Si-Mg with higher iron content, Manufacturing Technology 18 (4) (2018) 650–654.
[42] J. Zou, H. Zhang, C. Yu, Z. Wu, C. Guo, H. Nagaumi, K. Zhu, B. Li, J. Cui, Investigating the influences of Fe, Mn and Mo additions on the evolution of microstructure and mechanical performances of Al–Si–Mg cast alloys, J. Mater. Res. Technol. 25 (2023) 319–332.
[43] M. Tash, F.H. Samuel, F. Mucciardi, H.W. Doty, Effect of metallurgical parameters on the hardness and microstructural characterization of as-cast and heat-treated 356 and 319 aluminum alloys, Mater. Sci. Eng., A 443 (1) (2007) 185–201.
[44] L. Lu, A.K. Dahle, Iron-rich intermetallic phases and their role in casting defect formation in hypoeutectic Al—Si alloys, Metall. Mater. Trans. A 36 (13) (2005) 819–835.
[45] M.S. Remøe, K. Marthinsen, I. Westermann, K. Pedersen, J. Røyset, C. Marioara, The effect of alloying elements on the ductility of Al-Mg-Si alloys, Mater. Sci. Eng., A 693 (2017) 60–72.